



Molecular Structure of Kerogen in the Longmaxi Shale: Insights from Solid State NMR, FT-IR, XRD and HRTEM

WANG Xiaoqi^{1,2}, ZHU Yanming^{1,2,*}, LIU Yu^{1,2} and LI Wu^{1,2}

¹ Key Laboratory of Coalbed Methane Resources and Reservoir Formation on Process, Ministry of Education, China University of Mining and Technology, Xuzhou 221008, Jiangsu, China

² School of Resources and Geosciences, China University of Mining and Technology, Xuzhou 221116, Jiangsu, China

Abstract: Kerogen plays an important role in shale gas adsorption, desorption and diffusion. Therefore, it is necessary to characterize the molecular structure of kerogen. In this study, four kerogen samples were isolated from the organic-rich shale of the Longmaxi Formation. Raman spectroscopy was used to determine the maturity of these kerogen samples. High-resolution transmission electron microscopy (HRTEM), ¹³C nuclear magnetic resonance (¹³C NMR), X-ray diffraction (XRD) and Fourier transform infrared (FT-IR) spectroscopy were conducted to characterize the molecular structure of the shale samples. The results demonstrate that $V_{R_{eqv}}$ of these kerogen samples vary from 2.3% to 2.8%, suggesting that all the kerogen samples are in the dry gas window. The macromolecular carbon skeleton of the Longmaxi Formation kerogen is mainly aromatic ($f_a^* = 0.56$). In addition, the aromatic structural units are mainly composed of naphthalene (23%), anthracene (23%) and phenanthrene (29%). However, the aliphatic structure of the kerogen macromolecules is relatively low ($f_{al}^* + f_{al}^H = 0.08$), which is presumed to be distributed in the form of methyl and short aliphatic chains at the edge of the aromatic units. The oxygen-containing functional groups in the macromolecules are mainly present in the form of carbonyl groups ($f_a^C = 0.23$) and hydroxyl groups or ether groups ($f_a^O = 0.13$). The crystallite structural parameters of kerogen, including the stacking height ($L_c = 22.84 \text{ \AA}$), average lateral size ($L_a = 29.29 \text{ \AA}$) and interlayer spacing ($d_{002} = 3.43 \text{ \AA}$), are close to the aromatic structural parameters of anthracite or overmature kerogen. High-resolution transmission electron microscopy reveals that the aromatic structure is well oriented, and more than 65% of the diffractive aromatic layers are concentrated in the main direction. Due to the continuous deep burial, the longer aliphatic chains and oxygen-containing functional groups in the kerogen are substantially depleted. However, the ductility and stacking degree of the aromatic structure increases during thermal evolution. This study provides quantitative information on the molecular structure of kerogen samples based on multiple research methods, which may contribute to an improved understanding of the organic pores in black shale.

Key words: organic-rich shale, molecular structure, kerogen, HRTEM, Sichuan Basin

Citation: Wang et al., 2019. Molecular Structure of Kerogen in the Longmaxi Shale: Insights from Solid State NMR, FT-IR, XRD and HRTEM. Acta Geologica Sinica (English Edition), 93(4): 1015–1024. DOI: 10.1111/1755-6724.13870

1 Introduction

Shale gas is an important unconventional gas resource (Zou Caineng et al., 2016). In recent years, a considerable number of studies detailing shale reservoir characteristics and shale gas accumulation processes have demonstrated that the micropores in shale play a vital role in shale gas storage and transport. The nanoscale organic pores, which contribute to the largest part of the total pore volume, are the main storage space for shale gas (Wang Min et al., 2016). Meanwhile, it is well documented that some nanoscale organic pores (<2 nm) are formed within the three-dimensional (3D) molecular structure, and their pore structure parameters are controlled by the molecular composition and spatial structure of the organic matter (Bousige et al., 2016; Huang et al., 2017; Vasileiadis et al., 2017; Liu et al., 2018a). Therefore, the evaluation of gas storage and transport is strengthened by a robust

understanding of the molecular structure of the organic matter.

Great advances have been achieved in the characterization of kerogen chemical structure (Requejo et al., 1992; Vandembroucke and Largeau, 2007; Longbottom et al., 2017). The evolution of the kerogen structure in shale has been the focus of previous studies (Vandembroucke and Largeau, 2007). It is well known that aliphatic chains and oxygen containing groups continue to decrease with increasing maturity, and the aromaticity of the kerogen molecular structure increases from immature kerogen to overmature kerogen (Kelemen et al., 2007; Wang et al., 2013; Pernia et al., 2015; Zhao et al., 2016; Lai et al., 2017). In other words, the aliphatic groups and oxygen containing groups are tailored down from the kerogen structure during thermal evolution (Pernia et al., 2015; Zhao et al., 2016; Lai et al., 2017). In addition, with increasing maturity, the ordering degree increases and basic structural units become locally parallel (Romero-Sarmiento et al., 2014).

* Corresponding author. E-mail: ymzhucumt@126.com

When investigating the molecular structure of kerogen, different kinds of techniques are usually used, such as element analysis, solid-state ^{13}C nuclear magnetic resonance (NMR) spectroscopy and Fourier transform infrared (FT-IR) spectroscopy (Vandenbroucke and Largeau, 2007). Several kerogen structural models have been built based on the qualitative or semiquantitative information provided by these methods (Requejo et al., 1992; Orendt et al., 2013; Craddock et al., 2017; Gao et al., 2017; Hackley et al., 2017; Longbottom et al., 2017; Stock et al., 2017). In addition, these 3D kerogen models have been used in methane adsorption and micropore structure analysis (Huang et al., 2017). However, the orientation and ordering degree of the aromatic layers, regarded as important spatial position information on the kerogen structure, has been ignored in most of the existing 3D kerogen models (Vandenbroucke and Largeau, 2007; Bousige et al., 2016; Huang et al., 2017). Some studies have been performed on the structural alignment of coal (Mathews and Sharma, 2012; Romero-Sarmiento et al., 2014). Due to the complexity and heterogeneity of kerogen, it is still a big challenge to build a realistic 3D kerogen model considering the orientation of the aromatic layers.

The Longmaxi shale in the Sichuan Basin is the focus of shale gas exploration and exploitation in China (Zou et al., 2016). Extensive research detailing the shale reservoir characteristics has shown that the thermal maturity of the Longmaxi shale is highly mature with equivalent the vitrinite reflectance ranging between 2.0 and 4.5% (Dai et al., 2014). The different types and levels of maturity, documented by the molecular models of kerogen in other shales cannot be directly applied to the kerogen in the Longmaxi shale. Huang et al. proposed an average molecular model of the organic matter in the Longmaxi shale based on the structural parameters provided by Fourier transform infrared (FTIR) spectroscopy (Huang et al., 2017). Unfortunately, few studies have concentrated on the crystallite structure characterization of kerogen in the Longmaxi shale because crystallites have a greater effect on the micropore structure in organic matter.

The major aim of this study is to understand the chemical structure of the kerogen in the Longmaxi Formation. Four kerogen samples from the Longmaxi Formation were isolated. ^{13}C nuclear magnetic resonance (^{13}C NMR), X-ray diffraction (XRD) and Fourier transform infrared (FT-IR) spectroscopy were employed to characterize the crystallite structure and chemical structure of the kerogen in the Longmaxi Formation. Raman spectroscopy experiments were also employed to characterize the thermal maturity of kerogen. In addition, high-resolution transmission electron microscopy (HRTEM) was conducted to analyse the chemical structure and to better understand the structural alignment of the kerogen samples.

2 Geological Settings

The shale samples in this study were collected from the Longmaxi Formation in the southern part of the Sichuan Basin, which is considered the most successful gas shale in China (Zou et al., 2016; Wei et al., 2017). Four black shale samples were collected from the Xiaoxi section and Fendong section (Fig. 1), and there is no fracture or magma intrusion in these two sections. The basic information of the sample is shown in Table 1. The TOC contents of all samples are higher than or equal to 1.8%. Meanwhile, the dominant mineralogical compositions of the studied samples are quartz, calcite and clay in descending order of abundance.

3 Samples and Methods

In this study, four kerogen samples were separated from the organic-rich shale of the Longmaxi Formation using a chemical method. After sample preparation, Raman spectroscopy was used to determine the maturities of these kerogen samples. Then, high-resolution transmission electron microscopy (HRTEM), ^{13}C nuclear magnetic resonance (^{13}C NMR), X-ray diffraction (XRD) and Fourier transform infrared (FT-IR) spectroscopy were conducted to characterize the molecular structures of these shale samples. The detailed description of each experiment is contained in the following sections.

3.1 Sample preparation

Kerogen separation was performed based on the Chinese national standard method (GB/T19144-2010). Initially, 500-g shale samples were crushed to gravel-size particles smaller than 1 mm³ using an agate mortar before isolation. Next, HCl and HF were used to remove the carbonate and silicate minerals, respectively. The samples were then treated with zinc particles and HCl to remove the pyrite in the shale. Finally, centrifugation was performed to separate the kerogens. More details can be found in Chinese National Standard GB/T19144-2010 (isolation method for kerogen from sedimentary rock). We performed microscopic identification of the extracted kerogen. To determine the kerogen type, we also calculated the TI index according to the percentage of the organic microscopic composition according to the following formula. More details can be found in Chinese Oil and Gas Industry Standard SY/T5125-1996 (identification and classification of kerogen microscopic components).

$$TI = MB + 0.5E - 0.75V - I \quad (1)$$

where *MB* is sapropelite, *E* is exinite, *V* is vitrinite, and *I* is inertinite.

The remaining kerogen samples were pulverized to a size smaller than 300 mesh before the subsequent experiments were conducted.

Table 1 Basic information of the sample

Sample	TOC	TI	Kerogen type	Quartz	Potash feldspar	Plagioclase	Calcite	Dolomite	Pyrite	Clay
X-3	6.7	95	I	43.40	1.70	5.50	22.10	4.20	1.9	21.2
X-5	9.9	93	I	77.00	3.00	4.00	-	-	-	16.0
F-3	4.1	89	I	65.00	1.00	1.00	16.00	8.00	-	9.0
F-11	1.8	98	I	32.00	0.60	4.70	13.10	29.30	2.60	17.7

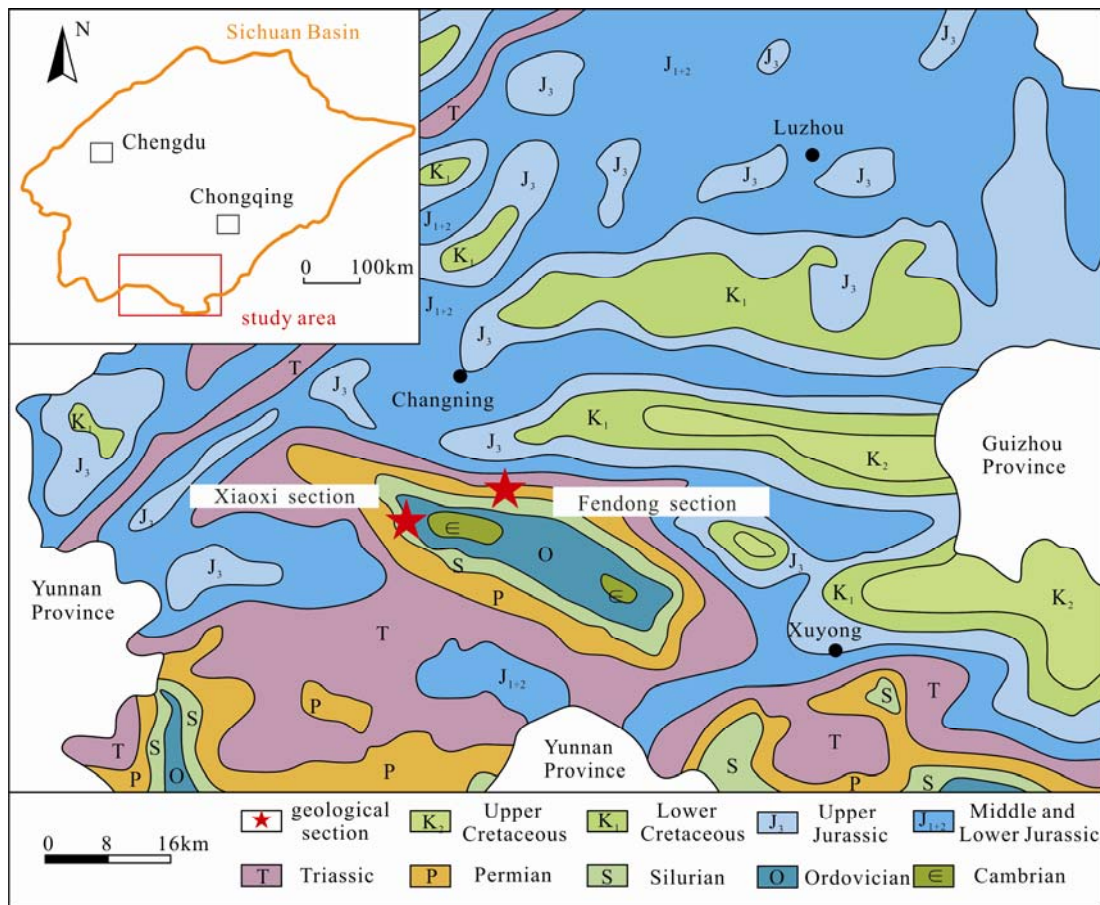


Fig. 1. Shale sample collection location from Sichuan Basin.

3.2 Raman experiment

In this work, Raman experiment was performed using a Raman spectroscopy microscope Senterra produced by Bruker Company (Germany). The experimental laser wavelength was 532 nm. The integration time was 2 seconds. The range of the scan wavenumber was 45–4500 cm^{-1} .

The equivalent vitrinite reflectance (VR_{eqv}) was adopted as an important parameter for representing the thermal evolution stage of organic matter in the shale (Sauerer et al., 2017). However, organic matter particles in shale are rare and relatively small in diameter, bringing great difficulty in measuring the VR_{eqv} directly. In recent years, it has been found that there is an intimate connection between the microcrystallite structure and the Raman spectrum (Wilkins et al., 2014). Raman spectrograms have been successfully used to calculate the VR_{eqv} of kerogen in shale (Liu Dehan et al., 2013; Wilkins et al., 2014). Raman curves with wave numbers between 1000–2000 cm^{-1} were fitted and exhibited two major peaks (D peak and G peak) (Fig. 2). The basic Raman spectrum parameters of each shale sample are shown in Table 1. These parameters are calculated from the peak positions and peak intensities of the G and D peaks (Fig. 2). Then, VR_{eqv} can be calculated by Eq. 2 (Wilkins et al., 2014).

$$VR_{eqv} = -3.291 + 7.432 \log(v_G - v_D) - 0.306 \log(\text{saddle index}) - 2.935 \log(FWHM^G) - 3.118 \log(FWHM^D) \quad (2)$$

where $(v_G - v_D)$ is the difference between the central positions of the G and D bands; the saddle index is the

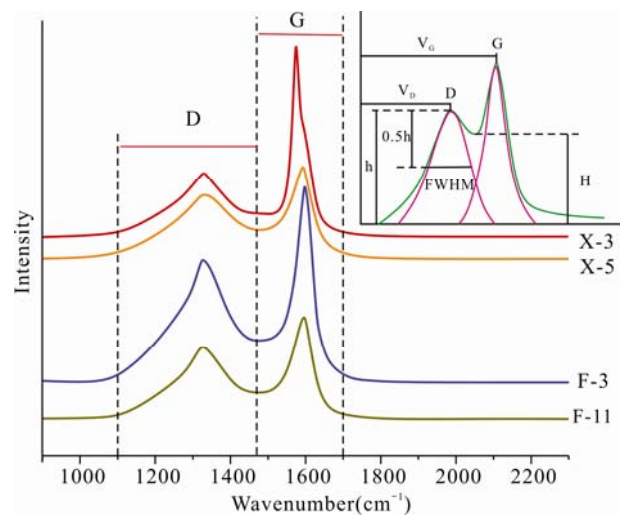


Fig. 2. Raman spectra and Raman band identification.

ratio of the height of the G band to the minimum height between the G and D bands; and $FWHM^G$ and $FWHM^D$ are the full widths at the half mean for the G band and D band, respectively.

3.3 Solid-State Cross-Polarization Magic-Angle Spinning (CP/MAS) ^{13}C NMR Analysis

The ^{13}C NMR spectra were measured using a Bruker

Avance III 400 spectrometer produced by Bruker Company (United States). To allow the experiments to run in the double-resonance probe head, 4 mm sample rotors were used. The NMR experiment was conducted at the Institute of Coal Chemistry, Chinese Academy of Sciences. The NMR parameters were calculated through the peak fitting method according to previous studies (Okolo et al., 2015; Song et al., 2017) (Table 2). It is noteworthy that we also calculated the ratio of aromatic bridge carbon to aromatic peripheral carbon ($X_{BP}=f_a^B/(f_a^H+f_a^P+f_a^S)$), which is an indicator of the size of the aromatic structural unit (BSU)(Song et al., 2017).

Table 2 NMR parameters and carbon assignment determined by NMR data

Carbon assignment	NMR shift (δ)	Fraction of total carbon (symbols)
carbonyl group or carboxyl group	>165	f_a^C
aromatic carbon bonded to hydroxyl or ether oxygen	150-165	f_a^P
alkylated aromatic carbon	135-150	f_a^S
aromatic bridgehead carbon	130-135	f_a^B
protonated and aromatic carbon	90-130	f_a^H
aliphatic C bonded to oxygen	60-90	f_{al}^O
aliphatic CH or CH ₂	25-60	f_{al}^H
aliphatic CH ₃ or quaternary carbon	0-25	f_{al}^*

3.4 X-ray diffraction(XRD) experiment

The XRD experiments were conducted at the Advanced Analysis and Computation Center of China University of Mining and Technology. A D8 ADVANCE, produced by Bruker Company (Germany), was employed to collect the XRD data. The operating conditions of the X-ray tube were U=40 kV and I=30 mA. The XRD curve is usually divided into 100 and 002 peaks in vitrinite coal and shale kerogen(Takagi et al., 2004). These two peaks correspond to the 2θ range of 15–30° and 40–50°, respectively. The crystallite structural parameters, including interlayer spacing (d_{002}), average lateral size (L_a), and stacking height (L_c), are considered as measures of the perfection of the stacking structure periodicity(Takagi et al., 2004). These three parameters can be calculated by the following formula based on the XRD data (Eq. 3 to Eq. 5) (Li et al., 2013; Wu and Zhu, 2014).

$$d_{002}(\text{Å}) = \lambda/2\sin\theta_{002} \quad (3)$$

$$L_c(\text{Å}) = 0.9\lambda/(\beta_{002}\cos\theta_{002}) \quad (4)$$

$$L_a(\text{Å}) = 1.84\lambda/(\beta_{100}\cos\theta_{100}) \quad (5)$$

where λ is the wavelength of the X-ray (Å); θ_{002} and θ_{100} are the peak positions of the 002 and 100 bands(°); and β_{002} and β_{100} are the peak widths at the half heights of 002 and 100 bands(rad), respectively.

3.5 Fourier transform infrared (FT-IR) experiment

The FT-IR experiments were performed on the Fourier Transform Infrared Spectroscopy Vertex 80v instrument

produced by Bruker Company (Germany). In the FT-IR experiment, the KBr pellet technique was used. After the KBr and kerogen samples were mixed well, the mixed samples were loaded into a mould and pressurized to 90 KN/cm² under vacuum. Then, Fourier transform infrared spectroscopy was used to obtain the FT-IR spectra of these kerogen samples. The recorded spectra ranged from 400 to 4000 cm⁻¹ and the resolution was 0.06 cm⁻¹.

3.6 High-resolution transmission electron microscopy (HRTEM) experiment

In this study, the HRTEM experiments were conducted at the China University of Mining and Technology using a FEI/20 Field Emission Electron Microscope. A high-quality 200 mesh copper micro-grid was used to hold the kerogen particles. Then, these particles were observed using the Field Emission Electron Microscope. Noisewave in Photoshop software was used to reduce the noise in all the HRTEM images. The white fringes in these micrographs represent the aromatic rings (Niekerk and Mathews, 2010). All the fringes have been assigned to different ring size groups that were false colored according to the assignments established by Mathews and his co-workers (Niekerk and Mathews, 2010; Mathews and Sharma, 2012).

4 Results

4.1 The maturity of the kerogen based on the Raman data

It was found by microscopic identification of the kerogen that the TI value of all the samples was greater than or equal to 89 (Table 1), suggesting that they were all type I kerogen (SY/T5125-1996). The final calculation results of the VR_{eqv} are shown in Table 3. The VR_{eqv} value of the Longmaxi Formation shale was between 2.33 and 2.78% with an average of 2.58%. It is noteworthy that the VR_{eqv} of the Fendong section was slightly larger than that of the Xiaoxi section. In general, the statistical range of the VR_{eqv} parameters was less than 20% of their average, indicating that there was little difference in the kerogen maturity between the two sections.

4.2 Chemical structure through the 13C-NMR and FT-IR spectra

The ¹³C-NMR spectra of the kerogen were mainly composed of three parts: aliphatic parts (shift: 0–90 ppm), aromatic parts (shift: 100–156 ppm) and carbonyl carbon parts (shift: 165–220 ppm) (Fig. 3). The parameters corresponding to these three parts were f_a' , f_a^C and f_{al} in descending order of their value. Among these, f_a' displayed the maximum value, ranging from 0.51 to 0.59, with an average of 0.55 (Table 4). f_a^C was between 0.21 and 0.26, with an average of 0.23 (Table 4). f_{al} varied from

Table 3 Raman spectrum basic parameters

Sample	V_D	V_G	RBS (cm ⁻¹)	H a.u.	$FWHM$ (cm ⁻¹)	$FWHM^G$ (cm ⁻¹)	VR_{eqv} (%)
X-3	1325	1575	250	303.20	55	152.5	2.33
X-5	1326	1594.5	268.5	390.44	52.6	174	2.57
F-3	1328.5	1599	270.5	366.66	46	165	2.78
F-11	1331.5	1595	263.5	351.19	49.6	161.6	2.65

Note: RBS is the difference between the central positions of the G and D bands; H is the minimum height between the G and D bands; $FWHM^G$ and $FWHM^D$ are the full widths at the half mean for G the band and D band, respectively.

0.18 to 0.24, with an average of 0.21 (Table 4). In addition, the average value of X_{BP} was 0.36, ranging from 0.25 to 0.42 (Table 4). Overall, the statistical range of the NMR parameters was less than 24% of their average, indicating that there was little difference in the NMR parameters between the four samples.

Figure 4 shows the FT-IR spectra of the kerogen samples. In general, these kerogen samples had similar spectral features. There were considerable absorbance intensities in the regions of 850–700 cm^{-1} (assigned to aromatic C-H), 1000–1300 cm^{-1} (assigned to C-O stretching) and 1550–1650 cm^{-1} (assigned to aromatic C=C stretching vibrations of the aromatic rings). Many differences also existed in the FT-IR spectra among these kerogen samples. Specifically, there were two obvious peaks located at 1725 and 3500 cm^{-1} in kerogen sample X-5, which were assigned to aliphatic C-O, -COOH and -OH stretching vibrations (Fig. 4). However, these two

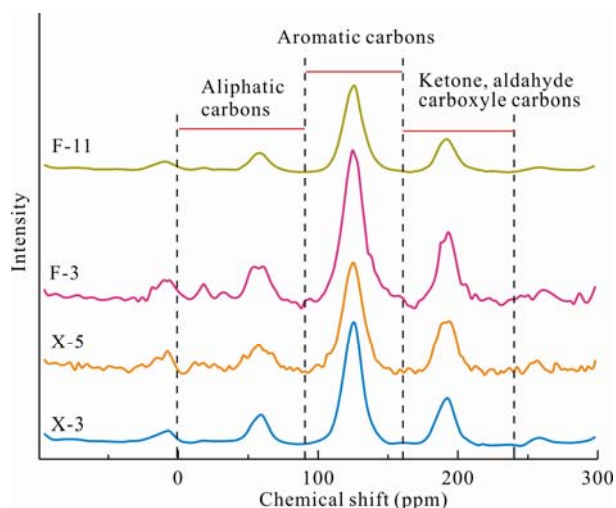


Fig. 3. NMR curves of the kerogen samples.

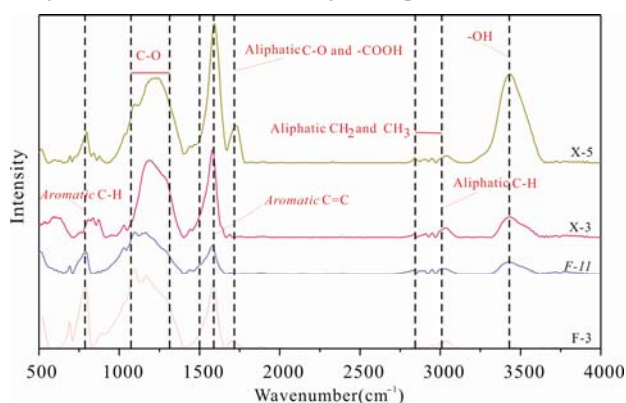


Fig. 4. FT-IR spectra of the Longmaxi Formation kerogen.

peaks were no longer obvious in the other kerogen samples. It is noteworthy that the intensity of the peaks located in the regions of 2800–3000 cm^{-1} (assigned to aliphatic C-H stretching vibration and symmetric aliphatic CH_2 and CH_3 stretching vibration) was quite weak in all the kerogen samples.

4.3 Crystallite structure through the XRD curves and HRTEM images

The XRD curves showed that these kerogen samples had similar spectral features, except for the larger 001 peak amplitude of sample F-11 related to the other samples (Fig. 5). In general, the intensities of the 100 peaks of the kerogen samples were much weaker than those of the 002 peaks. It is noteworthy that the XRD curves had several sharp peaks of small magnitude, indicating that a small fraction of the mineral had remained unremoved. However, they did not affect the calculation of the crystallite structure parameters. Table 5 shows that d_{002} ranged from 3.40 to 3.45 Å, with an average of 3.42 Å. L_c was between 16.38 and 27.50 Å, with an mean of 22.84 Å. Additionally, L_a varied from 23.66 to 35.21 Å, with an average of 29.29 Å.

Figure 6 illustrates HRTEM micrographs of these four kerogen samples. Heterogeneities existed in the distributions of the different sized aromatic rings (Fig. 7). The quantitative data of the aromatic rings revealed that the naphthalene rings, 2×2-sized rings and 3×3-sized rings contributed most the total aromatic rings (Fig. 8). Among these, the 3×3-sized rings occupied the largest proportion, with an average of 0.29. Quantitative analysis shows that the fringes were highly oriented, with more than 65% of the total fringes in the major direction (Fig. 9).

5 Discussions

5.1 Thermal evolution stage of the Longmaxi Formation

The VR_{eqv} calculation results reveal that the kerogen of the Longmaxi Formation reached the stage of overmaturity. The evolution of the aromatic structures and aliphatic structures were the main causes of the changes in Raman spectrum parameters during maturation (Su Xianbo et al., 2016; Wang Maolin et al., 2015). A detailed discussion of the chemical structure characterization of kerogen in the Longmaxi Formation will be carried out in Section 4.2. Su Xianbo et al. (2016) found that the function of aromatization, aromatic ring condensation and sp² fold lead to the rapid decrease of $FWHM^D$. The RBS reaches its maximum at the end of aromatic ring condensation. The value of $FWHM^D$ and RBS in this study suggest that the organic matter of the Longmaxi Formation shale is in the process of transition from

Table 4 NMR parameters and carbon assignment determined by NMR data

Sample	f_a	f_a^C	f_a^I	f_a^N	f_a^H	f_a^P	f_a^S	f_a^B	f_{al}	f_{al}^*	f_{al}^H	f_{al}^O	X_{BP}
X-3	0.82	0.22	0.59	0.16	0.44	0.00	0.00	0.16	0.18	0.03	0.02	0.13	0.36
X-5	0.79	0.26	0.52	0.15	0.37	0.00	0.00	0.15	0.21	0.05	0.03	0.13	0.41
F-3	0.76	0.24	0.50	0.18	0.33	0.02	0.07	0.10	0.24	0.05	0.05	0.14	0.25
F-11	0.79	0.21	0.58	0.22	0.36	0.00	0.04	0.17	0.21	0.00	0.09	0.13	0.42

Note: f_a - total aromatic carbon; f_a^C - carbonyl; f_a^I - aromatic ring; f_a^N - non-protonated and aromatic; f_a^H - protonated and aromatic; f_a^P - phenolic; f_a^S - alkylation aromatic; f_a^B - aromatic bridgehead; f_{al} - total aliphatic carbon; f_{al}^* - CH_3 or non-protonated; f_{al}^H - CH or CH_2 ; f_{al}^O - bonded to oxygen. $X_{BP} = f_a^B / (f_a^H + f_a^P + f_a^S)$.

aromatic ring condensation to spell fold function (Figs. 10, 11).

5.2 Chemical structure characterization of kerogen in Longmaxi Formation

High values of f_a' (average=0.55) compared with f_a^c (average=0.23) and f_{al} (average=0.21) suggest that the aromatic carbon in the kerogen of the Longmaxi Formation is the main structural component. Moreover, the values of X_{BP} (average=0.36) are similar to the results of anthracite (Liu et al., 2018b), likely reflecting that the aromatic core structure is dominated by 3 to 4 or larger aromatic rings according to the pattern described by Song (2017). The number of aromatic rings in the core of the

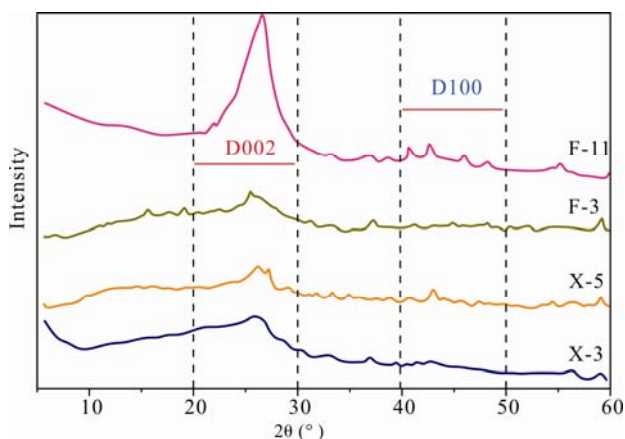


Fig. 5. XRD profiles of the kerogen samples.

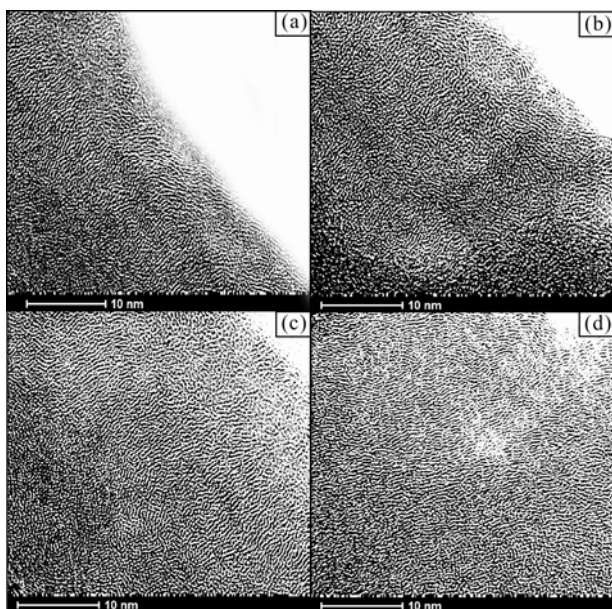


Fig. 6. HRTEM images of the shale kerogen samples(a: X-3; b: X-5; c: F-3; d: F-11).

Table 5 Crystallite structure parameters of the kerogen

Sample	$2\theta_{100}(\circ)$	$2\theta_{002}(\circ)$	$\beta_{002}(\text{rad})$	$\beta_{100}(\text{rad})$	$d_{002}(\text{Å})$	$L_c(\text{Å})$	$L_a(\text{Å})$
X-3	43.6	25.8	0.09	0.13	3.45	16.38	23.66
X-5	45.2	26.2	0.05	0.09	3.40	27.50	35.21
F-3	44.5	25.9	0.07	0.12	3.44	22.42	25.83
F-11	43.8	26.1	0.06	0.09	3.41	25.07	32.44

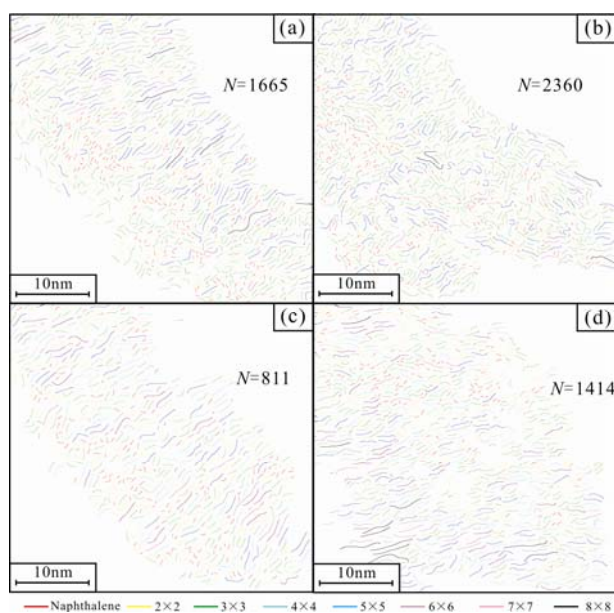


Fig. 7. False colored fringes from HRTEM micrographs of the kerogen samples (a: X-3; b: X-5; c: F-3; d: F-11; N represents the number of fringes).

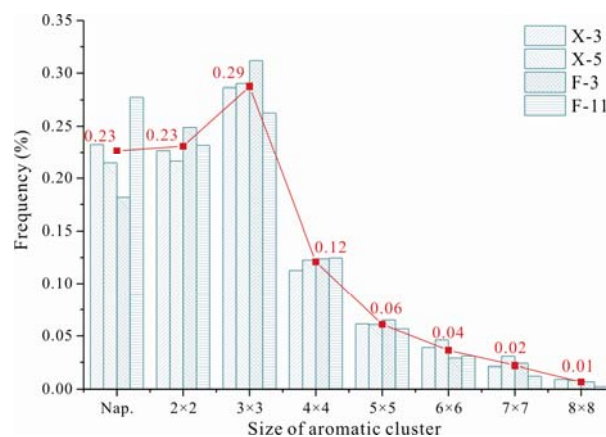


Fig. 8. Frequency distribution of the different aromatic fringe groups in the kerogen samples.

basic structural unit increases sharply with increasing maturation (Kelemen et al., 2007; Wang et al., 2013; Pernia et al., 2015; Zhao et al., 2016; Lai et al., 2017). The size of the aromatic rings can be directly counted based on HRTEM images (Mathews and Sharma, 2012; Liu et al., 2018b). Therefore, we discuss the aromatic rings in more detail in Section 4.3, where f_{al}^O is the largest in the aliphatic carbon parameters with an average of 0.13. The average f_{al}^H and f_{al}^* values are only 0.05 and 0.03, respectively. Such a composition of f_{al} may reflect that the aliphatic part played a role in the connection between the aromatic carbon in the kerogen macromolecules of the Longmaxi Formation.

Three obvious peaks of the FT-IR spectra in the kerogen samples described earlier suggest that the aliphatic skeletal C-O, aromatic C-H and aromatic C=C comprised most of the total macromolecular structure (Fig. 6). However, the weak peaks assigned to aliphatic

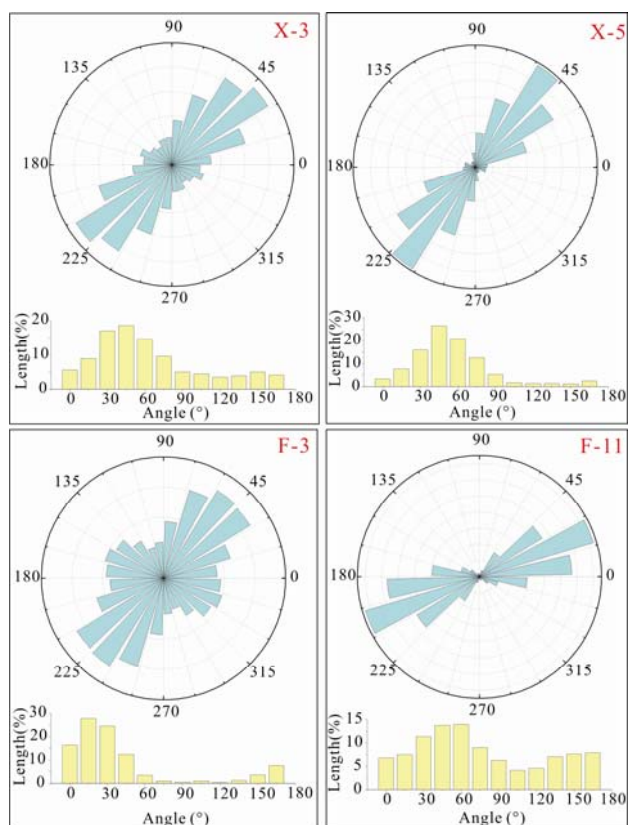


Fig. 9. Angle distribution of the aromatic fringes from the HRTEM micrographs.

stretching vibration reflected a lower aliphatic carbon content. In general, the abovementioned speculation of the chemical structure through FT-IR spectra corresponded with those obtained through ^{13}C -NMR, suggesting that the skeleton of the macromolecular structure appeared to be composed of aromatic rings in kerogen of the Longmaxi formation.

Previous studies indicated that many aliphatic chains are tailored down from the molecular structure due to petroleum generation during maturation (Pernia et al., 2015; Zhao et al., 2016; Lai et al., 2017). Continuous aliphatic carbon loss was observed throughout the pyrolysis experiment with the f_{al} value decreasing from 0.636 at a VR_{eqv} value of 0.6% to 0.079 at VR_{eqv} 1.6% (Gao et al., 2017). Similarly, Kelemen et al. (2007) found that f_{al} decline from 0.54 to 0.18 between immature kerogen and post-mature kerogen. In contrast, the trend of f_a is opposite to f_{al} during maturation. The value of f_a increased continuously from 32.7% ($VR_{eqv}=0.60\%$) to 90.1% ($VR_{eqv}=1.6\%$) according to the experiments conducted by Gao et al. (2017). In addition, a similar trend was found by Kelemen et al. (2007) with a marked increase from 0.46 to 0.82 in the thermal maturity sequence between immature kerogen and post-mature kerogen. Remarkably, this relationship is virtually identical to that found for coal (Pernia et al., 2015; Zhao et al., 2016; Lai et al., 2017). Compared with these results, f_{al} and f_a in this study agreed well with the value of post-mature kerogen reported by Kelemen et al. (2007). In addition, the VR_{eqv} calculation

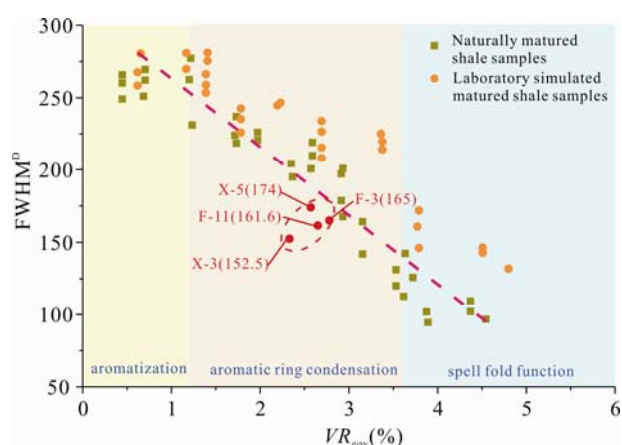


Fig. 10. Relationship between $FWHM^D$ and VR_{eqv} (naturally matured and laboratory matured shale samples are cited from Wang et al., 2015).

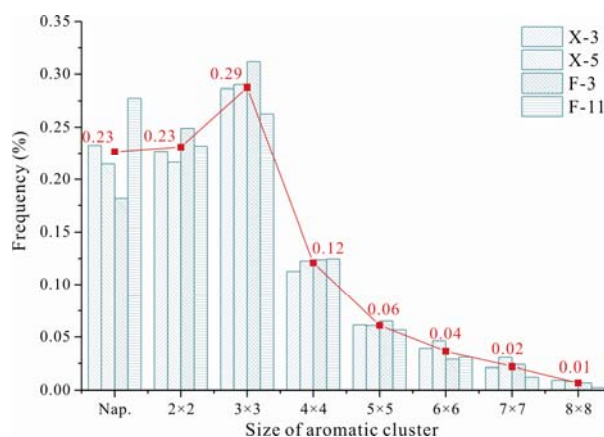


Fig. 11. Relationship between RBS and VR_{eqv} (naturally matured and laboratory matured shale samples are cited from Wang et al., 2015).

results suggested that all the kerogen samples in our study were in the dry gas window. Therefore, we imply that the functional groups had experienced evolutionary paths in which the aliphatic chains were shortened and the degree of aromaticity was enhanced during the thermal maturation of the kerogen.

5.3 Crystallite structure and the structural alignment of the kerogen in the Longmaxi Formation

The parameters, d_{002} , L_a and L_c , represent the inter-layer spacing, crystallite diameter and crystallite height, respectively (Lu et al., 2001; Li et al., 2013; Okolo et al., 2015). Generally, the above three crystallite structural parameters are closely related to the maturity of the organic matter, as indicated by XRD data in previous studies (Sharma et al., 1999; Sharma et al., 2000; Takagi et al., 2004). Liu et al. (2018b) found that the values of d_{002} dropped sharply from 0.386 nm ($R_o=0.60\%$) to a minimum of 0.351 nm ($R_o=2.1\%$) and increased slightly from the minimum to 0.355 nm ($R_o=4.2\%$). However, the trend of L_a and L_c is opposite to d_{002} during maturation. The relationship between L_a and R_o was observed by Liu et al. (2018b), with a marked increase from 1.4 to 2.8 in

the interval of R_o between 0.60 and 2.9% and a slower decrease after $R_o > 2.90\%$. Similarly, the value of L_c increased continuously from 0.7 ($R_o=0.60$) to a maximum of 1.8 ($R_o=2.0$) and decreased from the maximum to 1.3 ($R_o=4.2\%$) according to the experiments conducted by Liu et al. (2018b). The values of d_{002} , L_a and L_c in this study agreed well with the values of anthracite reported by Liu et al. (2018b). The lower d_{002} values and higher L_c values (Table 3 and Fig. 12) indicate a larger number of aromatic layers in the stacking structure of the Longmaxi Formation kerogen. The crystallite structures evolved towards the features of graphite, decreasing the inter-layer spacing and increasing the crystallite diameter and crystallite height (d_{002} for graphite is 3.35 Å) (Takagi et al., 2004).

The above results of the crystallite structures calculated through the XRD curves could also be obtained from the HRTEM experiment (Sharma et al., 1999). However, it is not possible to know which aromatic layer belongs to which stacking number from XRD analysis (Sharma et al., 2000). The dominant size of the aromatic rings, obtained from HRTEM images was consistent with that calculated through XRD. Recent research results indicate that the sizes of aromatic rings are continuously enlarged with increasing maturity (Mathews and Sharma, 2012; Liu et al., 2018a). Liu et al. (2018a) found that the proportions of aromatic rings larger than 3×3 increased from 1% ($VR_{eqv} = 0.60\%$) to 50% ($VR_{eqv} = 3.2\%$). However, the aromatic ring content smaller than 3×3 decreased from 81 to 18% in the same VR_{eqv} interval. The layer size distribution was in good agreement with the results from the HRTEM analysis of overmature kerogen samples analysed by Liu et al. (2018a). In addition to calculating the size distribution of the aromatic layers, the HRTEM images could provide information about the spatial alignment of the kerogen structures. Remarkably, there was a

significant difference among the spatial alignments of the immature, mature, and overmature kerogen samples. In particular, the proportions of aromatic rings in the major direction of the overmature kerogen samples were much larger than those of the immature and mature kerogen samples. In other words, better alignment could be observed in the overmature kerogen samples than in the immature and mature kerogen samples. Compared with these results, the proportions of aromatic rings in the major direction in this study (Fig. 11) agreed well with the values of the overmature kerogen samples reported by Liu et al. (2018a).

It is noteworthy that the scale of the HRTEM image in this study was $20 \text{ nm} \times 20 \text{ nm}$. Due to the heterogeneity and complexity of the kerogen structure, the quantitative data obtained from the HRTEM images may not be representative of the sample in general. Therefore, we are now in the process of observing more spots, which will be reported soon.

5.4 Macromolecular structure evolution of the kerogen in the Longmaxi Formation

The organic-rich shale experienced long-term deep burial after the deposition of the Longmaxi Formation in the southern part of the Sichuan Basin (Chen et al., 2017). During the late Yanshanian, the bottom burial depth of the Longmaxi Formation reached the maximum depth (greater than 6000 m), and the highest heating temperature of organic matter was greater than or equal to 200°C (Fig. 12). Accordingly, the maturation level was greater than 2.3%, and all the kerogen samples were in the dry gas window. In addition, the macromolecular structure of the kerogen varied based on the burial history and hydrocarbon generation. The longer aliphatic structures and oxygen-containing functional groups in the kerogen

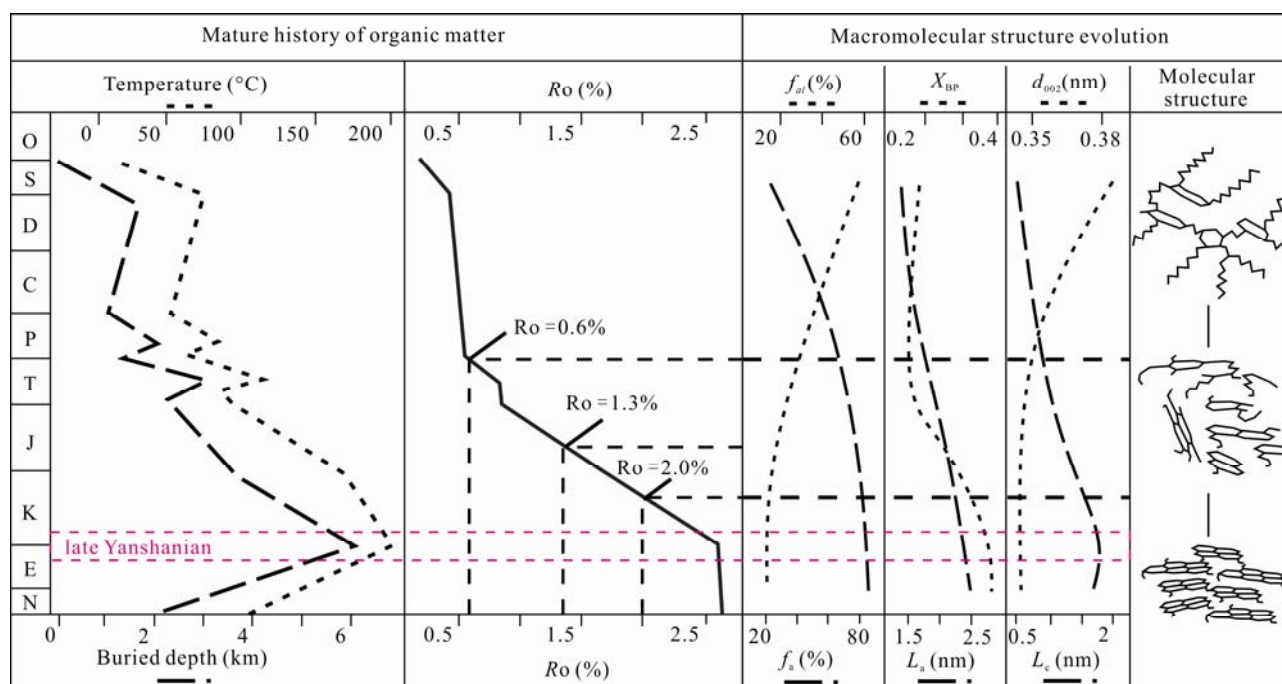


Fig. 12. Burial history of the Longmaxi Formation and evolution of the kerogen macromolecular structure (the burial history as modelled by Chen et al. (2017). The macromolecular structure parameters as reported by Liu et al. (2018b))

were substantially depleted during thermal evolution. (Pernia et al., 2015; Zhao et al., 2016; Lai et al., 2017) The aromatic ring formed a large aromatic structural unit through aromatization, ring condensation and folding, which not only significantly enhanced the rank physicochemical degree between the kerogen aromatic structural units, but also led to the increase in ductility and stacking degree of the aromatic structure (Kelemen et al., 2007; Wang et al., 2013; Pernia et al., 2015; Zhao et al., 2016; Lai et al., 2017). Thus, the kerogen molecules has similar structural features as anthracite.

With increasing maturation, both the chemical molecular composition and crystallite structure change and thus have great effects on the micropore (<2 nm) structure in the organic matter (Radovic et al., 1997; Zhu and Sheng, 2010; Feng et al., 2013; Liu et al. 2018b). Micropores in low mature organic matter are mainly related to aliphatic parts. Whereas, The micropores in highly mature organic matter are mainly formed between the planes of aromatic rings or between the edges of different aromatic layers (Liu et al., 2018b). Consequently, the micropores related to the aromatic rings are plane-shaped and have good connections (Liu et al., 2018b). The abovementioned results agree with the Longmaxi Formation shale having reached the stage of overmature evolution, and its structure is close to that of anthracite. As a result, the organic matter pores in the kerogen should be mostly associated with the aromatic structure. Furthermore, a better crystallite alignment contributes to the formation of smaller micropores (Radovic et al., 1997; Zhu and Sheng, 2010; Liu et al., 2018b). The micropore volume was found to increase abruptly in the range of $R_o=1.4-4.0\%$, although the aromatic carbon rate did not show significant changes (Liu et al., 2018b). Due to the limitation of the experimental methods for direct observation of the internal pores in organic matter, detailed information on the microstructure of the kerogen was not obtained. More details may be discussed in future studies.

6 Conclusions

The following conclusions can be drawn:

(1) The V/R_{eqv} value of the Longmaxi Formation shale is between 2.33% and 2.78%. All the kerogen samples are in the dry gas window.

(2) The macromolecular carbon skeleton structure of the Longmaxi Formation kerogen is mainly aromatic. The aromatic structural units are mainly composed of naphthalene, anthracene and phenanthrene. The aliphatic structure of the kerogen macromolecules is relatively small, which is presumed to be distributed in the form of methyl and short aliphatic chains at the edge of aromatic units. The oxygen-containing functional groups in the macromolecules are mainly present in the form of carbonyl groups and hydroxyl groups or ether groups.

(3) The crystallite structural parameters of the kerogen, including L_c , L_a and d_{002} , are close to the aromatic structural parameters of anthracite. The aromatic structure was well oriented, and more than 65% of the diffractive aromatic layers were concentrated in the main direction.

(4) Due to the continuous deep burial, the longer

aliphatic chains and oxygen-containing functional groups in the kerogen are substantially depleted. In addition, the ductility and stacking degree of the aromatic structure increase during thermal evolution. The micropores in the kerogen are mostly associated with the aromatic structure. In addition, better crystallite alignment may contribute to the formation of micropores.

Acknowledgements

This work is supported by the National Science and Technology Major Project (2017ZX05035004-002), the National Natural Science Foundation of China (no. 41702167), and the Fundamental Research Funds for the Central Universities (No.2017CXNL03), and the Scientific Research Foundation of the Key Laboratory of Coalbed Methane Resources and Reservoir Formation Process, Ministry of Education (China University of Mining and Technology) (No. 2017-007).

Manuscript received Oct. 14, 2018
accepted Nov. 13, 2018
associate EIC HAO Ziguo
edited by FEI Hongcai

References

- Bousige, C., Ghimbeu, C.M., Vix-Guterl, C., Pomerantz, A.E., Suleimenova, A., Vaughan, G., Garbarino, G., Feyngenson, M., Wildgruber, C., Ulm, F., Pellenq, R., and Coasne, b., 2016. Realistic molecular model of kerogen's nanostructure. *Nature Materials*, 15(5): 576–582.
- Chen, S., Zhu, Y., Chen, S., Han, Y., Fu, C., and Fang, J., 2017. Hydrocarbon generation and shale gas accumulation in the Longmaxi Formation, Southern Sichuan Basin, China. *Marine and Petroleum Geology*, 86: 248–258.
- Craddock, P.R., Prange, M., and Pomerantz, A.E., 2017. Kerogen thermal maturity and content of organic-rich mudrocks determined using stochastic linear regression models applied to diffuse reflectance IR Fourier transform spectroscopy (DRIFTS). *Organic Geochemistry*, 110: 122–133.
- Feng, Y., Jiang, C., Liu, D., and Chu, W., 2013. Experimental investigations on microstructure and adsorption property of heat-treated coal chars. *Journal of Analytical and Applied Pyrolysis*, 104: 559–566.
- Dai, J., Zou, C., Liao, S., Dong, D., Ni, Y., Huang, J., Wu, W., Gong, D., Huang, S., and Hu, G., 2014. Geochemistry of the extremely high thermal maturity Longmaxi shale gas, southern Sichuan Basin. *Organic Geochemistry*, 74: 3–12.
- Gao, Y., Zou, Y.R., Liang, T., and Peng, P.A., 2017. Jump in the structure of Type I kerogen revealed from pyrolysis and ^{13}C DP MAS NMR. *Organic Geochemistry*, 112(2017): 105–118.
- Hackley, P.C., Walters, C.C., Kelemen, S.R., Mastalerz, M., and Lowers, H.A., 2017. Organic petrology and micro-spectroscopy of Tasmanites microfossils: applications to kerogen transformations in the early oil window. *Organic Geochemistry*, 114(2017): 23–24.
- Huang, L., Ning, Z., Wang, Q., Qi, R., Li, J., Zeng, Y., Ye, H., and Qin H., 2017. Thermodynamic and structural characterization of bulk organic matter in Chinese Silurian Shale: Experimental and molecular modeling studies. *Energy & Fuels*, 31(5): 4851–4865.
- Kelemen, S.R., Afeworki, M., Gorbaty, M.L., Sansone, M., Kwiatek, P.J., Walters, C.C., Freund, H., and Siskin, M., 2007. Direct characterization of kerogen by X-Ray and Solid-State ^{13}C Nuclear Magnetic Resonance methods. *Energy & Fuels*, 21(3): 1548–1561.
- Lai, D., Zhan, J.H., Tian, Y., Gao, S., and Xu, G., 2017. Mechanism of kerogen pyrolysis in terms of chemical

- structure transformation. *Fuel*, 199: 504–511.
- Li, M., Zeng, F., Chang, H., Xu, B., and Wang, W., 2013. Aggregate structure evolution of low-rank coals during pyrolysis by in-situ X-ray diffraction. *International Journal of Coal Geology*, 116(5): 262–269.
- Liu, D.H., Xiao, X.M., Tian, H., Min, Y.S., Zhou, Q., Cheng, P., and Shen J., 2013. Sample maturation calculated using Raman spectroscopic parameters for solid organics: Methodology and geological applications. *Science Bulletin*, 58(11): 1285–1298.
- Liu, Y., Zhu, Y., Chen, S., Wang, Y., and Song, Y., 2018a. Evaluation of spatial alignment of kerogen in shale using High-Resolution Transmission Electron Microscopy, Raman Spectroscopy and Fourier Transform Infrared. *Energy & Fuels*, 32(10): 10616–10627.
- Liu, Y., Zhu, Y., Chen, S., Liu, W., and Wang, Y. 2018b. Molecular structure controls on micropore evolution in coal vitrinite during coalification. *International Journal of Coal Geology*, 199: 19–30.
- Longbottom, T.L., Hockaday, W.C., Boling, K.S., and Dworkin, S.I., 2017. Effect of ocean oxidation on the chemical structure of marine kerogen. *Organic Geochemistry*, 106: 1–12.
- Lu, L., Sahajwalla, V., Kong, C., and Harris, D., 2001. Quantitative X-ray diffraction analysis and its application to various coals. *Carbon*, 39(12): 1821–1833.
- Mathews, J.P., and Sharma, A., 2012. The structural alignment of coal and the analogous case of Argonne Upper Freeport coal. *Fuel*, 95(1): 19–24.
- Niekerk, D.V., and Mathews, J.P., 2010. Molecular representations of Permian-aged vitrinite-rich and inertinite-rich South African coals. *Fuel*, 89(1): 73–82.
- Okolo, G.N., Everson, R.C., Neomagus, H.W.J.P., Roberts, M.J., and Sakurovs, R., 2015. Comparing the porosity and surface areas of coal as measured by gas adsorption, mercury intrusion and SAXS techniques. *Fuel*, 141(141): 293–304.
- Orendt, A.M., Pimienta, I.S.O., Badu, S.R., Solum, M.S., Pugmire, R.J., and Facelli, J.C., 2013. Three-Dimensional structure of the Siskin Green River oil shale kerogen model: A comparison between calculated and observed properties. *Energy & Fuels*, 27(2): 702–710.
- Pernia, D., Bissada, K.K., and Curiale, J., 2015. Kerogen based characterization of major gas shales: Effects of kerogen fractionation. *Organic Geochemistry*, 78: 52–61.
- Radovic, L.R., 1997. On the porous structure of coals: evidence for an interconnected but constricted micropore system and implications for coalbed methane recovery. *Adsorption*, 3(3): 221–232.
- Requejo, A.G., Gray, N.R., Freund, H., Thomann, H., Melchior, M.T., Gebhard, L.A., Pictroski, C.F., and Hsu, C.S., 1992. Maturation of petroleum source rocks. 1. Changes in kerogen structure and composition associated with hydrocarbon generation. *Energy & Fuels*, 6(2): 203–214.
- Romero-Sarmiento, M.F., Rouzaud, J.N., Bernard, S., Deldicque, D., Thomas, M., and Littke, R., 2014. Evolution of Barnett Shale organic carbon structure and nanostructure with increasing maturation. *Organic Geochemistry*, 71(6): 7–16.
- Sauerer, B., Craddock, P.R., Aljohani, M.D., Alsamadony, K.L., and Abdallah, W., 2017. Fast and accurate shale maturity determination by Raman spectroscopy measurement with minimal sample preparation. *International Journal of Coal Geology*, 173: 150–157.
- Sharma, A., Kyotani, T., and Tomita, A., 1999. A new quantitative approach for microstructural analysis of coal char using HRTEM images. *Fuel*, 78(10): 1203–1212.
- Sharma, A., Kyotani, T., and Tomita, A., 2000. Comparison of structural parameters of PF carbon from XRD and HRTEM techniques. *Carbon*, 38(14): 1977–1984.
- Song, Y., Zhu, Y., and Li, W., 2017. Macromolecule simulation and CH₄ adsorption mechanism of coal vitrinite. *Applied Surface Science*, 396: 291–302.
- Stock, A.T., Littke, R., Schwarzbauer, J., Horsfield, B., and Hartkopf-Fröder, C., 2017. Organic geochemistry and petrology of Posidonia Shale (Lower Toarcian, Western Europe) – The evolution from immature oil-prone to overmature dry gas-producing kerogen. *International Journal of Coal Geology*, 176: 36–48.
- Su, X.B., Si, Q., and Song, J.X., 2016. Characteristics of coal Raman spectrum. *Journal of China Coal Society*, 41(5): 1197–1202 (in Chinese with English abstract).
- Takagi, H., Maruyama, K., Yoshizawa, N., Yamada, Y., and Sato, Y., 2004. XRD analysis of carbon stacking structure in coal during heat treatment. *Fuel*, 83(17): 2427–2433.
- Vandenbroucke, M., and Largeau, C., 2007. Kerogen origin, evolution and structure. *Organic Geochemistry*, 38(5): 719–833.
- Vasileiadis, M., Peristeras, L.D., Papavasileiou, K.D., and Economou, I.G., 2017. Modeling of bulk kerogen porosity: Methods for control and characterization. *Energy & Fuels*, 31(6): 6004–6018.
- Wang, Q., Lu, H., Greenwood, P., Shen, C., Liu, J., and Peng, P., 2013. Gas evolution during kerogen pyrolysis of Estonian Kukersite shale in confined gold tube system. *Organic Geochemistry*, 65(6): 74–82.
- Wang, M.L., Xiao X.M., Wei, Q., and Zhou, Q., 2015. Thermal maturation of solid bitumen in Shale as revealed by Raman spectroscopy. *Natural Gas Geoscience*, 26(9): 1712–1718 (in Chinese with English abstract).
- Wang, M., Lu, S.F., Wang, Z.W., Liu, Y., Huang, W.B., Chen, F.W., and Xu, X.Y., 2016. Reservoir characteristics of lacustrine shale and marine shale: examples from the Songliao Basin, Bohai Bay Basin and Qiannan depression. *Acta Geologica Sinica (English Edition)*, 90(3): 1024–1038.
- Wei, X.F., Zhao, Z.B., Wang, Q.B., Liu, Z.J., Zhou, M., and Zhang, H., 2017. Comprehensive evaluation on geological conditions of the shale gas in Upper Ordovician Wufeng Formation-Lower Silurian Longmaxi Formation in Dingshan Area, Qijiang, Southeastern Sichuan. *Geological Review*, 63(01): 153–164 (in Chinese with English abstract).
- Wilkins, R.W.T., Boudou, R., Sherwood, N., and Xiao, X., 2014. Thermal maturity evaluation from inertinites by Raman spectroscopy: The ‘RaMM’ technique. *International Journal of Coal Geology*, 128–129: 143–152.
- Wu, L., and Zhu, Y., 2014. Structural characteristics of coal vitrinite during pyrolysis. *Energy & Fuels*, 28(6): 3645–3654.
- Zhao, T.T., Ge, W.Z., Nie, Y.X., Wang, Y.X., Zeng, F.G., and Qiao, Y., 2016. Highly efficient detoxification of Cr (VI) by brown coal and kerogen: Process and structure studies. *Fuel Processing Technology*, 150: 71–77.
- Zhu, X., and Sheng, C., 2010. Evolution of the char structure of lignite under heat treatment and its influences on combustion reactivity. *Energy & Fuels*, 24(1): 152–159.
- Zou, C.N., Yang, Z., Pan, S.Q., Chen, Y.Y., Lin, S.H., Huang, J.L., Wu, S.T., Dong, D.Z., Wang, S.F., Liang, F., Sun, S.S., Huang, Y., and Weng, D.W., 2016. Shale gas formation and occurrence in China: An overview of the current status and future potential. *Acta Geologica Sinica (English Edition)*, 90(4): 1249–1283.

About the first author



WANG Xiaoqi, male, born in 1994 in Zhangjiakou City, Hebei Province; PhD student at China University of Mining and Technology. His main research includes the characteristics of shale gas reservoirs and resource evaluation. Address: Nanhu Campus, China University of Mining and Technology, No. 1 University Road, Xuzhou City, Jiangsu Province, 221116. E-mail: 1030086301@qq.com.

About the corresponding author



ZHU Yanming, male, born in 1963 in Danyang City, Jiangsu Province; Ph.D.; graduated from China University of Mining and Technology. His main research includes the characteristics of shale gas reservoirs and resource evaluation. Address: Nanhu Campus, China University of Mining and Technology, No. 1 University Road, Xuzhou City, Jiangsu Province, 221116. E-mail: ymzhucumt@126.com.